Three-dimensional point spread function and generalized amplitude transfer function of near-field flat lenses

Carlos J. Zapata-Rodríguez,[1,*] David Pastor,[1] and Juan J. Miret[2]

[1]Departamento de Óptica, Universidad de Valencia, Dr. Moliner 50, 46100 Burjassot, Spain

[2]Departamento de Óptica, Universidad de Alicante, P.O. Box 99, Alicante, Spain

*Corresponding author: carlos.zapata@uv.es

Received 21 July 2010; revised 9 September 2010; accepted 19 September 2010; posted 21 September 2010 (Doc. ID 131940); published 18 October 2010

We derive a nonsingular, polarization-dependent, 3D impulse response that provides unambiguously the wave field scattered by a negative-refractive-index layered lens and distributed in its image volume. By means of a 3D Fourier transform, we introduce the generalized amplitude transfer function in order to gain a deep insight into the resolution power of the optical element. In the near-field regime, fine details containing some depth information may be transmitted through the lens. We show that metamaterials with moderate absorption are appropriate for subwavelength resolution keeping a limited degree of depth discrimination.

OCIS codes: 100.6640, 160.3918, 240.6680, 310.6628.

1. Introduction

The possibility of recovering subwavelength details of an object is a subject of growing interest leading to a profusion of superresolving image-forming techniques. In 2000, Pendry showed that a thin slab of a medium with negative refractive index (NRI) is capable of generating a exact replica of a plane object, thus being coined as a perfect lens [1]. This idea was previously conceived by Veselago, based on simple ray tracing [2]. For the homogeneous part of the field, a phase reversal is accomplished within the NRI medium that compensates the phase gathered by the wave when traveling away from the source. On the other hand, the evanescent components of the wave field carrying those subwavelength features are amplified in the metamaterial layer in order to regain their amplitudes at the image plane. To do it, coupled surface plasmons are excited at the input and output interfaces of the NRI material slab [3–5]. Unfortunately, absorption inherent in NRI media restrains a perfect lens from ideal reconstruction of the object. Experimental evidence of NRI imaging was early found in microwaves [6–8]; however, this challenge remains for higher frequencies.

To derive the limit of resolution, the amplitude transfer function (ATF) of the system has been preferably examined, since it directly provides the cutoff frequency beyond which one cannot find any spectral component in the reconstructed image. For simplicity, the analysis is commonly carried out at the image plane of line sources leading to a $(1+1)D$ problem [4,5,9,10]. Thus, separating the s-polarized and p-polarized components of the field, the image-forming metamaterial layer behaves as a linear and shift-invariant system having a scalar transfer function. Silver superlenses and metal-dielectric multilayer stacks have also exploited this sort of 1D spectral analysis [11–13].

In a complementary procedure, what may be adopted is the Rayleigh criterion of resolution for which two point sources are just resolved when the first diffraction minimum of the image of one point object coincides with the maximum of the adjacent source [14]. The electric dipole antenna is the most

0003-6935/10/305870-08$15.00/0

well-accepted model for line [15,16] and point sources [17], leading a complete description of the focal waves in the image volume. In these cases, however, the orientation of the electric dipole plays a key role in the resolution of the imaging system.

Seemingly more appropriate, the point spread function (PSF) itself may be referred to as a resolution gauge for our optical element since the full width of its central peak may be used to estimate the limit of resolution. This assessment must be taken with care, since high-frequency components in the phase of a blurred PSF might lead to the reproduction of the object details much finer than the FWHM of the PSF [13]. In particular, the response of the imaging slab for each polarization may be developed by means of the PSF, resulting from the Fourier transform of the corresponding ATF. Nieto-Vesperinas showed that the 3D behavior of this impulse response is singular in loss-free perfect imaging [10]. For band-limited near-field image formers, however, the out-of-focus field distribution is regularized at least along finite distances [18].

Furthermore, in optical microscopy, we generally have nonplanar objects leading to the analysis of point sources placed at different distances from the image-forming device. In this case, we identify distinct limits of resolution along a direction either parallel or perpendicular to the lens facets [19]. Specifically, the transverse resolution has been studied in detail, but little is said about the axial resolution of these layered metamaterial lenses.

Let us provide here a complete analysis of the resultant wave field reproduced in the image space of a near-field metamaterial thin lens, as the field is fully prescribed in terms of the 3D PSF. The geometric form of the PSF shall assist us in estimating the resolution power of the imaging device in three dimensions.

This paper is organized as follows. In Section 2, the basic grounds on image formation in NRI thin slabs are reviewed, adding emphasis to the function of its impulse response. In Section 3, we introduce the generalized ATF as the 3D Fourier transform of the PSF. We identify a closed-surface sheet for the far field and a hyperboloid sheet for the evanescent wave component. From the geometry of the generalized ATF, we interpret the PSF pattern in the image volume. Moreover, this allows us to provide in Section 4 some relevant aspects on the depth-discrimination capabilities of the perfect lens. Finally, in Section 5, the main conclusions are outlined.

2. Image Formation with NRI Slabs

Let us consider a thin metamaterial slab with its front face (input plane) at $z = 0$ and the output plane at $z = d$, thus d denoting the layer width. This optical element depicted in Fig. 1 will generate an image in the semispace $z \geq d$ from a given plane object lying on $z = -z_0 (z_0 \geq 0)$. For simplicity, we assume that both object and image media are the vacuum. To have a high-fidelity reproduction at the image plane, the negative index of refraction n_2 of the metamaterial should coincide in magnitude with that of the object (and image) medium ($n_1 = 1$). Material losses prevent from this ideal situation and we therefore assume a realistic, simple model, in which permittivity and permeability are of the form $\epsilon_2 = \mu_2 = -1 + i\delta$. Under these circumstances, perfect imaging cannot be achieved, since $n_2 = -1 + i\delta$. However, a good replica may be found at the plane $z = z_1$, where $z_1 = 2d - z_0$ if $\delta \ll 1$. Moreover, the condition $0 \leq z_0 \leq d$ leads to real images in $d \leq z \leq 2d$.

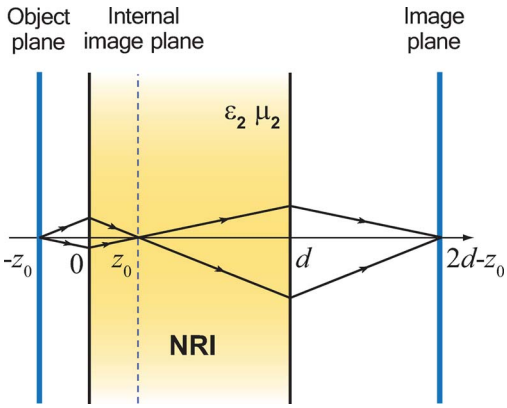

Fig. 1. (Color online) Schematic geometry of the planar-layer-based perfect lens.

In order to determine the wave fields in the image plane, it is customary to separate the s-polarized waves ($E_z = 0$) from the p-polarized waves ($H_z = 0$) constituting the electromagnetic field emitted by the source. From the analysis performed by Nieto-Vesperinas in Ref. [10], one may derive that the perfect lens is a linear and 3D shift-invariant system. It is not difficult to derive more general expressions, including material losses. For s-polarized waves, the transverse electric (TE) field emerging from the NRI slab satisfies (see Appendix A)

$$\vec{E}_{\text{out}}(\vec{R}, z) = \iint \vec{E}_{\text{in}}(\vec{R}_0, -z_0) h_3(\vec{R} - \vec{R}_0, z - z_1) \mathrm{d}^2\vec{R}_0, \tag{1}$$

where $\vec{E}_{\text{in}}(\vec{R}_0, -z_0)$ is the TE wave field at the object plane $\vec{R}_0 = (x_0, y_0)$ traveling in the direction of the input plane. We recognize the 3D function

$$h_3(\vec{R}, z) = \frac{1}{(2\pi)^2} \iint T(\vec{k}_\perp) \exp(i\vec{k}_\perp \vec{R} + i\beta_1 z) \mathrm{d}^2\vec{k}_\perp \tag{2}$$

as the PSF of the optical system. In Eq. (2), the transverse wave vector $\vec{k}_\perp = (k_x, k_y)$ and the layer transmittance

$$T(\vec{k}_\perp) = \frac{t_{12} t_{21} \exp[i(\beta_1 + \beta_2)d]}{1 - r_{21}^2 \exp(2i\beta_2 d)}, \tag{3}$$

follow the Airy formula [20] except for a linear phase factor. If $k_0 = 2\pi/\lambda_0$ denotes the wavenumber in vacuum, the propagation constant reads

$$\beta_j = \sigma_j \sqrt{k_0^2 \epsilon_j \mu_j - \vec{k}_\perp \cdot \vec{k}_\perp}, \quad \text{for } j = \{1,2\}. \tag{4}$$

Note that $\sigma_1 = 1$ for the vacuum and $\sigma_2 = -1$ for the NRI material. Also,

$$r_{jk} = \frac{\mu_k \beta_j - \mu_j \beta_k}{\mu_k \beta_j + \mu_j \beta_k} \tag{5}$$

is the coefficient of reflection for s-polarized waves at a single interface, and

$$t_{jk} = r_{jk} + 1. \tag{6}$$

For p-polarized waves, it is convenient to derive first the transverse magnetic (TM) field $\vec{H}_{\text{out}}(\vec{R}, z \geq d)$ from that TM field at the object plane $\vec{H}_{\text{in}}(\vec{R}_0, -z_0)$. This yields a convolution similar to Eq. (1), where its PSF may be written again into the plane-wave representation [Eq. (2)] by means of the layer transmittance [Eq. (3)]. It is well-known that the substitutions $\epsilon_j \leftrightarrow \mu_j$ switches the Airy formula for TM waves and TE waves, respectively [20]. In our case, however, both material parameters are set equal, providing a unique PSF.

Disregarding material losses ($\delta = 0$), we have $T = 1$ yielding $h_3(\vec{R}, 0) = \delta_2(\vec{R})$. In this limiting case [1], the presence of the 2D Dirac delta function δ_2 leads to a perfect image

$$\vec{E}_{\text{out}}(\vec{R}, 2d - z_0) = \vec{E}_{\text{in}}(\vec{R}_0, -z_0). \tag{7}$$

However, $h_3(\vec{R}, z)$ would exhibit a singular behavior in $z < 0$. From the Weyl's representation of the scalar Green's function, one may derive that [10]

$$h_3(\vec{R}, z < 0) = \frac{1}{2\pi} \frac{\partial}{\partial z} \left[\frac{\exp(-ik_0 r)}{r} \right], \tag{8a}$$

$$h_3(\vec{R}, z > 0) = -\frac{1}{2\pi} \frac{\partial}{\partial z} \left[\frac{\exp(ik_0 r)}{r} \right], \tag{8b}$$

where the distance from the point of observation,

$$\vec{r} = \vec{R} + z\hat{z}, \tag{9}$$

to the focal point located at the origin is $r = |\vec{r}|$. The role of δ consists of regularizing the out-of-focus field distribution given in Eq. (8a), thus providing a Wiener-like filter T.

The amplitude of the 3D PSF $|h_3|$ is depicted in Fig. 2 for NRI slabs of different widths d. Since T is radially symmetric, the PSF varies upon the axial coordinate z and the modulus of the transverse vector, R,

$$h_3(R, z) = \frac{1}{2\pi} \int_0^\infty T(k_\perp) J_0(k_\perp R) \exp(i\beta_1 z) k_\perp \mathrm{d}k_\perp, \tag{10}$$

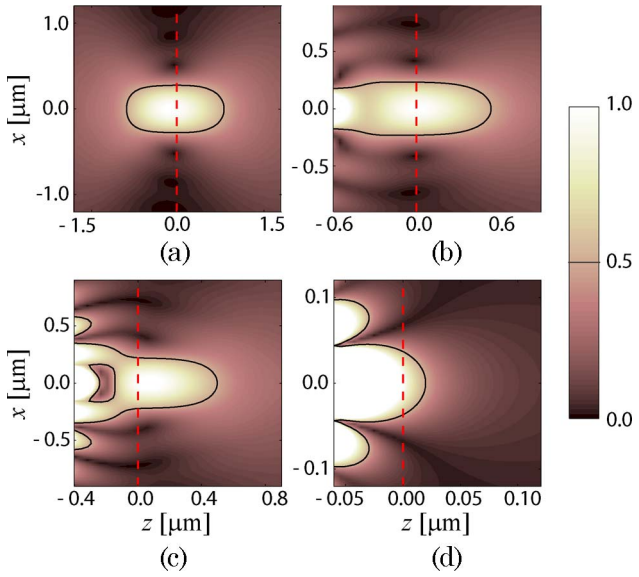

Fig. 2. (Color online) Absolute value of the PSF $|h_3|$ in $z \geq -d$ at $\lambda_0 = 600$ nm for absorbing slabs of $\delta = 0.1$ and different widths: (a) $d = 1.8$ μm, (b) $d = 600$ nm, (c) $d = 400$ nm, and (d) $d = 60$ nm. The plot is normalized to unity at $\vec{r} = 0$, and contour lines for a value 1/2 (solid line) are drawn in black. The image plane is now shifted to $z = 0$ (vertical red line).

where J_0 is a Bessel function of the first kind. In the numerical simulation, we set a wavelength $\lambda_0 = 600$ nm in vacuum, and losses $\delta = 0.1$ for the metamaterial. Shifting the image plane at $z = 0$, the exit surface of the layered lens would be found at $z = z_0 - d$. Bearing in mind that $z_0 \geq 0$, the meaningful part of the PSF lies within the range $z \geq -d$ as considered in the graphical representation. The 3D amplitude distribution of the PSF for a subwavelength width d shows a distinct behavior in comparison with those impulse responses for $d \gg \lambda_0$. For instance, the FWHM of the PSF at the image plane $\Delta_\perp = 73.5$ nm is clearly subwavelength if $d = 60$ nm; in fact, $\Delta_\perp$ would vanish if d were identically zero. Moreover, the amplitude reaches a maximum value at the center point $R = 0$ on the output plane. The response of the optical system points to that for near-field imaging. On the contrary, $\Delta_\perp = 552$ nm comes near the wavelength at $d = 1.8$ μm. Here, the maximum amplitude is found approaching the image plane far from the output plane, existing in a small longitudinal shift of 104 nm. Furthermore, one may determine a FWHM along the z axis, and in our case we found $\Delta_z = 1.70$ μm.

3. The Generalized ATF

It is well-known that a convenient interpretation of these results is derived by writing explicitly the far-field term and the evanescent wave term of the wave field. Here, it will be done for the 3D PSF given in Eq. (2). Within the spectral domain

$$\vec{k}_\perp \cdot \vec{k}_\perp = k_\perp^2 \leq k_0^2, \tag{11}$$

β_1 yields a real value leading to waves that carry energy to the far field $z \to \infty$. If $k_\perp > k_0$, however, β_1 is purely imaginary, so that this part of the wave field contributes exclusively to the near field $z \gtrsim z_0 - d$.

The 3D PSF given in Eqs. (2) and (10) is then written as

$$h_3(\vec{R}, z) = h_N(\vec{R}, z) + h_F(\vec{R}, z). \tag{12}$$

The far-field term may be represented as follows [21]:

$$h_F(\vec{R}, z) = \frac{-ik_0}{2\pi} \iint a(\vec{s}) \exp(ik_0 \vec{s}\vec{r}) \mathrm{d}\Omega. \tag{13}$$

Thus, h_F is evaluated from Eq. (2) within the far-field spectral domain, $0 \le \theta \le \pi/2$, being $d\Omega = \sin\theta d\theta d\phi$ the element of solid angle in spherical coordinates. In Eq. (13), the point of observation $\vec{r} = \vec{R} + z\hat{z}$ and the 3D unitary vector $\vec{s} = \vec{s}_\perp + s_z\hat{z}$ is deduced from the dispersion equation

$$k_0 \vec{s} = \vec{k}_\perp + \beta_1 \hat{z}. \tag{14}$$

Finally, the angular spectrum

$$a(\vec{s}) = \frac{i}{\lambda_0} T(\vec{s}) s_z, \tag{15}$$

where $s_z = \cos\theta$. Since $k_\perp = k_0 \sin\theta$, the transmittance T depends exclusively upon the azimuthal coordinate θ, and so does a.

The radiation intensity of a point source is in direct proportion with the squared absolute value of the angular spectrum, $|a(\theta)|^2$. The magnitude of the angular spectrum $|a|$ in the semispace $z > 0 (\theta < \pi/2)$ is plotted in Fig. 3 for superlenses analyzed in Fig. 2 of layer width (a) $d = 1.8$ μm, (b) $d = 600$ nm, (c) $d = 400$ nm, and (d) $d = 60$ nm. Material absorption attenuates the radiation intensity for increasing values of the slab width. However, the normalized radiation pattern is quite similar in all cases.

To gain a deep insight into the term h_F of the 3D PSF, let us consider the limiting case $\delta \to 0$. In this case, $T = 1$ and the transverse distribution of the PSF is an Airy disk,

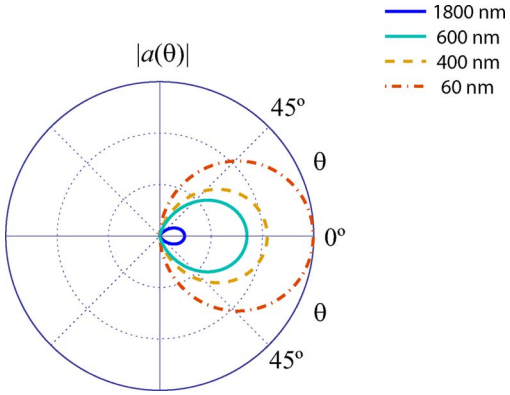

Fig. 3. (Color online) Absolute value of the angular spectrum in the semispace $z > 0$ associated with the 3D PSF for the superlenses analyzed in Fig. 2.

$$h_F(\vec{R}, 0) = \frac{J_1(k_0 R)}{\lambda_0 R}, \tag{16}$$

where J_1 is a Bessel function of the first kind. Along the axis $R = 0$, the nonevanescent 3D PSF may be expressed analytically as

$$h_F(0, z) = \frac{(1 - ik_0 z)\exp(ik_0 z) - 1}{2\pi z^2}. \tag{17}$$

This function is well-behaved in $z < 0$ so that, as expected, we encounter a singular response in the near-field term of the PSF. It is important to remark that $|h_F|$ in Eqs. (16) and (17) is maximum at the origin, whose central lobe has the FWHMs $\Delta_\perp = 0.705\lambda_0$ and $\Delta_z = 1.55\lambda_0$, respectively. At $\lambda_0 = 600$ nm, we have $\Delta_\perp = 423$ nm and $\Delta_z = 929$ nm. These numbers are roughly in agreement with the numerical simulation performed in Fig. 2(a) for $d = 1.8$ μm, revealing that h_F is the dominant part of the 3D PSF in this case. This is also true for higher values of d. Otherwise, the near-field component becomes significant (see subfigure for $d = 600$ and 400 nm), and even taking the control of the amplitude distribution in the image volume for slabs of a subwavelength width, as shown in Fig. 2(d).

We point out that h_F given in Eq. (13) represents a focused wave with focus at the origin $\vec{r} = 0$ and, as a consequence, it may follow the standard mathematical treatment of apertured spherical beams. In the limiting case $\delta = 0$, it yields an aberration-free focal wave, since $a(\vec{s})$ is a real function excepting a constant complex factor; otherwise, monochromatic aberrations arise [10,22].

Moreover, from Eq. (13), we infer that h_F may be written in terms of a 3D Fourier transform of the function $a(\vec{s})$, which has extent in three dimensions and is wrapped around the unit semisphere

$$\vec{s} \cdot \vec{s} = 1, \tag{18}$$

and $s_z \ge 0$ (see Fig. 4). In McCutchen's original paper [23], the function a is coined the "generalized aperture," describing the patch of solid angle occupied by the Huygenian source at the aperture plane of the converging wave. In our case, however, the transmitted amplitude is determined by the function T rather than the opacity on the exit pupil plane. Therefore, $a(\vec{s})$ is simply recalled as the generalized ATF of the NRI planar lens.

The near-field component of the wave field, h_N might be expressed in the form of Eq. (13) if the angular coordinate θ is represented in the complex plane. Setting $\theta = \pi/2 - i\alpha$ and running the real parameter α from 0 to ∞ allows us to consider the normalized wave vector $\vec{s}$ with real transverse component of modulus $s_\perp = \cosh\alpha > 1$ and the purely imaginary axial component $s_z = i\sinh\alpha$. The dispersion equation is

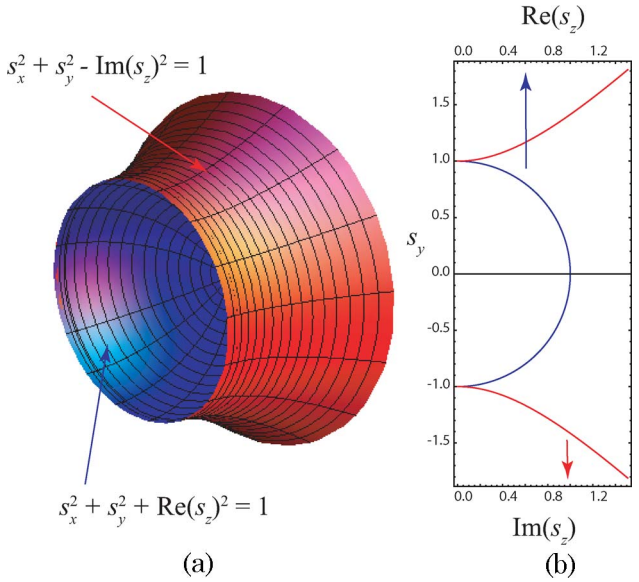

Fig. 4. (Color online) Spherical and hyperboloidal sheets constituting the generalized ATF are shown (a) in 3D and (b) on the meridional plane $s_x = 0$.

conveniently rewritten as $s_\perp^2 - (s_z'')^2 = 1$, representing a unit hyperboloid shown in Fig. 4, where $s_z'' = \mathrm{Im}(s_z)$ is the imaginary part of the on-axis projection of the wave vector. It is immediately derived that the angular spectrum $a(\vec{s})$ wrapped around the hyperboloid surface constitutes the second sheet of the generalized ATF associated with evanescent components of the wave field. Let us conclude as follows: the 3D PSF h_3 is fully computed by means of the 3D Fourier transform

$$h_F(\vec{r}) = \frac{-ik_0}{2\pi} \iint a(\vec{s}) \exp(ik_0 \vec{s}\vec{r}) \mathrm{d}^3\vec{s}, \qquad (19)$$

provided that the generalized ATF $a(\vec{s}) \equiv a(\vec{s})\delta(s-1)$, δ here is the Dirac delta function, and provided the real part and the imaginary part of s_z are nonnegative.

Previously, we mentioned that the 3D PSF h_3 is a singular function if the metamaterial lens is lossless, assuming that the absolute value of its negative refractive index is perfectly matched with that of the environment medium. This was predicted to be caused by the near-field term h_N. Such a singular behavior might be inferred now by considering the near-field term of the 3D ATF. The function $a(\vec{s})$ modulates the ATF over the hyperboloidal sheet. If $\delta \neq 0$, then $a(\vec{s})$ is effectively bounded, which leads to a 3D ATF representing an open surface of a finite area. Neglecting dissipation, however, a becomes unbounded, thus providing in the spectral domain a hyperboloid of infinite extent.

As shown in Fig. 5, the modulus $|a|$ is maximum at $\theta = 0$ for the far-field term, approaching $\lambda_0^{-1} \exp(-k_0 \delta d)$, and it decreases to zero at $\theta = \pi/2$. Within the near-field regime, $|a|$ grows exponentially at increasing values of α, however, attaining a local maximum $|a|_{\max}$ before it decreases for $\alpha \to \infty$. For

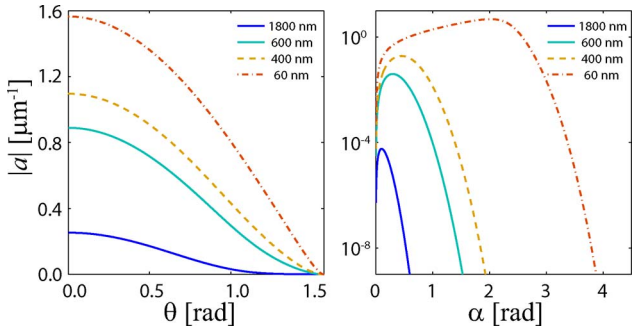

Fig. 5. (Color online) Absolute value of the angular spectrum $|a|$ for the numerical simulations of Fig. 2. The component of the far-field is represented in the subfigure on the left and the near-field term of the ATF is shown on the right.

$d = 60$ nm, the maximum $|a|_{\max} = 4.77\ \mu\mathrm{m}^{-1}$ at $\alpha_{\max} = 2.02$ rad, which corresponds to a normalized spatial frequency $s_\perp = 3.82$ (and $s_z = i3.69$). On the far-field sheet, the generalized ATF remains comparatively low, since $|a| \leq 1.57\ \mu\mathrm{m}^{-1} [= |a(\theta = 0)|]$. The effective area of the hyperboloidal surface, where $a(\vec{s})$ takes significant values, also surpasses in several units that from the unit semisphere. On the other hand, for $d = 1.8\ \mu$m, $|a|_{\max} = 5.7610^{-5}\ \mu\mathrm{m}^{-1}$ at $\alpha_{\max} = 0.104$ rad, associated with a unit vector of $s_\perp = 1.005$ (and $s_z = i0.104$). This is several orders of magnitude lower than the maximum $|a| = 0.253\ \mu\mathrm{m}^{-1}$ given at $\theta = 0$. Clearly, the effective area of $a(\vec{s})$ on the hyperboloid is here a fraction of that from the semisphere.

We conclude that the generalized ATF provides geometrical and analytical arguments in order to derive critically whether h_N represents the dominant contribution to the 3D PSF. This is of relevance, since the subwavelength resolution is achieved exclusively in such a case.

4. Depth of Field

Superresolving layered lenses made of metamaterials with realistic, moderate absorption are in practice limited by a subwavelength width. In this sense, a great effort has been made in order to provide wider stratified optical elements susceptible to reproduce subwavelength features [9,24,25]. For microscopy applications, an extended object should be confined in the vicinities of the NRI slab in order to give rise to real images. A quasi-planar source with grooves and small surface defects contains some depth information that might be transmitted through the lens. This issue is not evident, however, since the decay of the wave field from the output plane of the lens leads to inability for producing 3D focusing of energy in spots smaller than λ_0 [18].

As illustration, we show in Fig. 6 the contour plot of the field intensity in the image space of the near-field superlens analyzed in Fig. 2(c) as it is produced by two equienergetic point sources. An incoherent superposition is assumed to get rid of interference phenomena. Therefore, the intensity distribution is proportional to

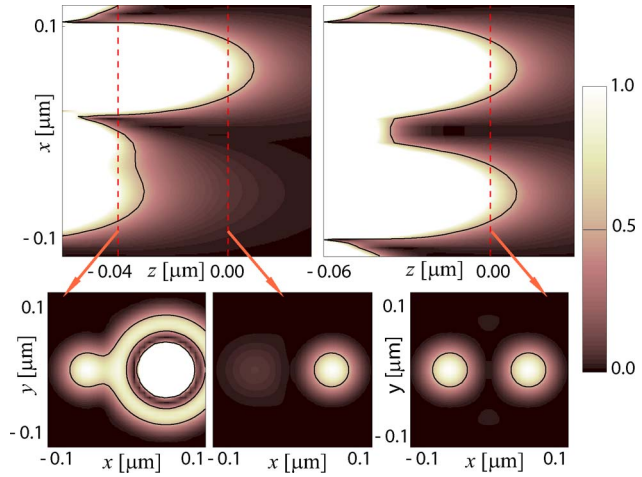

Fig. 6. (Color online) Intensity of the wave field in the image volume of two point sources centered at $\vec{R}'_1 = 60\hat{x}$ nm $= -\vec{R}'_2$ provided under different conditions of depth: (left) both sources are located in the same transverse plane and (right) one source is 40 nm closer to the lens. The layer width is $d = 60$ nm and material absorption is $\delta = 10^{-1}$.

$$\sum_{j=1,2} \left| h_3(\vec{R} - \vec{R}'_j, z - z'_j) \right|^2 . \tag{20}$$

This is consistent, for instance, with fluorescence microscopy under the first Born approximation [26]. Nevertheless, the output intensity of any pointlike source as an electric dipole antenna might be computed straightforwardly by inserting the appropriate field E_{in} rather than the Dirac delta function into Eq. (1). Both points are separated $|\vec{R}'_1 - \vec{R}'_2| =$ 120 nm along the transverse direction. We analyze the case that one of these objects O_1 stays closer to the lens than O_2, and therefore its image O'_1 remains in a plane (here, $z'_1 = 0$) farther from the lens back face. In this plane, the presence of the second image O'_2 is imperceptible in virtue of the evanescent nature of its wave field. Moving to the geometrical image plane of $O'_2 (z'_2 = -40$ nm), it is clearly detected, however, superposed to the strong back tail produced by O'_1.

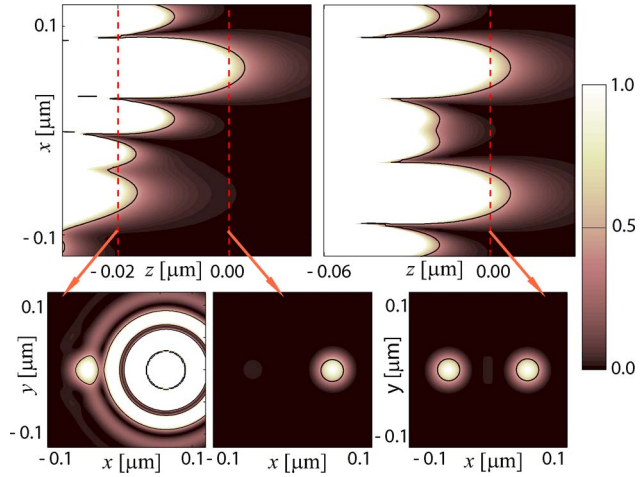

Fig. 7. (Color online) Same as in Fig. 6, considering a medium of lower loss $\delta = 10^{-2}$.

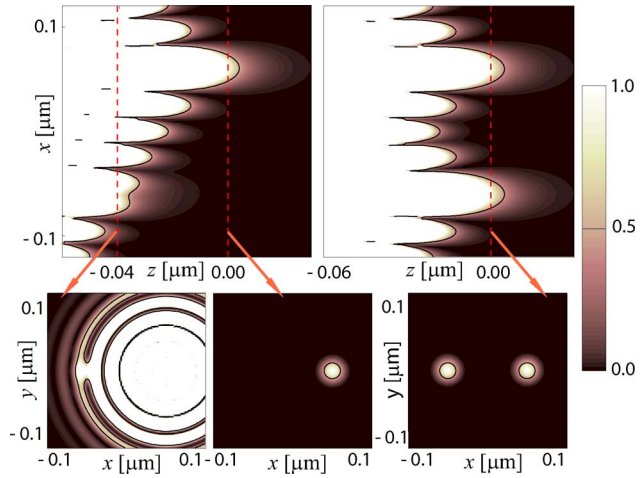

Fig. 8. (Color online) Same as in Fig. 6, for $\delta = 10^{-3}$.

In the case analyzed previously, out-of-focus sidelobes of the PSF attain a considerable strength leading to a fast image blurring and loss in resolution power. Following the half-maximum dashed line of the image intensity of O'_2 at its geometrical image plane z'_2 shown in Fig. 6, it also embodies the diffraction spot of O'_1 and, as a consequence, one may consider that both image points are not resolved. In order to increase the transverse resolution of the system, we represent in Fig. 7 its response for a more favorable value of the absorption parameter, $\delta = 10^{-2}$. Here, the half-maximum closed lines are separately associated with each impulse response of the two point sources. This superresolution mechanism relies exclusively on a decrement of the FWHM of the in-focus PSF of O'_2. In fact, the out-of-focus PSF of O'_1 has a larger FWHM.

From the discussion given above, one may infer that improving the resolution power of near-field NRI lenses is achieved at the cost of a fast image degradation in out-of-focus planes. Let us deeply examine this assessment with the help of Fig. 8. For an extremely low absorbing layer with parameter $\delta = 10^{-3}$, the lowest limit of resolution along the transverse direction (in-focus FWHM) is achieved in comparison with Figs. 6 and 7. Nevertheless, its back tail at $z < 0$ spreads much faster, hindering the observation of other images (O'_2) geometrically reproduced at the rear. Specifically, at z'_2, the radius of the out-of-focus diffraction spot associated with O'_1 goes beyond the gap $|\vec{R}'_1 - \vec{R}'_2|$ between this image and O'_2. This behavior becomes more evident as δ decreases and, more generally, if any physical mechanism improves the capability of the flat lens in resolving closer images placed in the same transverse plane.

5. Conclusions

In this paper, we exploit the properties of linearity and shift invariance featuring planar metamaterial superlenses. The wave field in the image volume replicates with unit magnification the 3D source distribution in front of the NRI slab. Therefore, the 3D distribution of the impulse response has

translational symmetry not only in a direction parallel to the layer facets, but also along the normal direction.

In direct analogy with conventional image-forming systems, we show that when a NRI planar lens produces an image of a point source, the 3D diffraction pattern that results is the 3D Fourier transform of a function that we called here the generalized ATF. This feasible application of the McCutchen analysis [23] relies on the relation between the angular spectrum of the PSF and the lens transmittance in the spatial-frequency domain. Thus, the generalized ATF includes two different sheets: one, having a spherical shape, contains information of the far field, whereas the evanescent components of the wave are associated with the hyperboloidal sheet of the ATF.

Particularly, subwavelength resolution is mostly determined by the modulation of the generalized ATF on the hyperboloidal sheet. In connection with this result, we have understood that increasing transverse resolution within the near-field regime may be produced at the cost of loss in depth discrimination. This feature is in opposition with far-field imaging, where only annular pupils limiting the transverse bandwidth of the ATF show an enhanced focal depth and, therefore, poor axial resolution [27,28].

Appendix A: Field Equations

Let us consider the single layer lens made of a left-handed metamaterial shown in Fig. 1. The TE field in the object space $z < 0$ is evaluated as the superposition of an incident wave field

$$\vec{E}_{\text{in}} = \iint \vec{A}(\vec{k}_\perp) \exp[i\vec{k}_\perp \vec{R} + i\beta_1(z + z_0)] \mathrm{d}^2\vec{k}_\perp, \quad \text{(A1)}$$

and the reflected field

$$\vec{E}_r = \iint R(\vec{k}_\perp)\vec{A}(\vec{k}_\perp) \exp[i\vec{k}_\perp \vec{R} - i\beta_1(z + z_0)] \mathrm{d}^2\vec{k}_\perp. \quad \text{(A2)}$$

The propagation constant β_1 is given in Eq. (4). In the plane-wave representation of the wave field, the spatial spectrum

$$\vec{A}(\vec{k}_\perp) = \frac{1}{(2\pi)^2} \iint \vec{E}_{\text{in}}(\vec{R}_0, -z_0) \exp(-i\vec{k}_\perp \vec{R}_0) \mathrm{d}^2\vec{R}_0 \quad \text{(A3)}$$

represents the 2D Fourier transform of the field propagating toward the superlens at the object plane $z = -z_0$. It is evident that $R(\vec{k}_\perp)$ stands for the coefficient of reflection for a s-polarized plane wave with transverse wave vector $\vec{k}_\perp$.

Inside the NRI slab ($0 < z < d$), the wave field is again a superposition of the propagating field

$$\vec{E}_{ts} = \iint T_s(\vec{k}_\perp)\vec{A}(\vec{k}_\perp) \exp[i\vec{k}_\perp \vec{R} + i\beta_2(z - z_0)] \mathrm{d}^2\vec{k}_\perp, \quad \text{(A4)}$$

and the counterpropagating field

$$\vec{E}_{rs} = \iint R_s(\vec{k}_\perp)\vec{A}(\vec{k}_\perp) \exp[i\vec{k}_\perp \vec{R} - i\beta_2(z - z_0)] \mathrm{d}^2\vec{k}_\perp. \quad \text{(A5)}$$

Finally, the field emerging from the imaging system in $z > d$ is determined by means of the equation

$$\vec{E}_{\text{out}} = \iint T(\vec{k}_\perp)\vec{A}(\vec{k}_\perp) \exp[i\vec{k}_\perp \vec{R} + i\beta_1(z - z_1)] \mathrm{d}^2\vec{k}_\perp. \quad \text{(A6)}$$

Boundary conditions at the input plane $z = 0$ and output plane $z = d$ lead to the evaluation of the coefficients R, T_s, R_s, and T. Thus, imposing continuity of the field $\vec{E}$ and its normal derivative $\mu^{-1}\partial_z\vec{E}$, we finally obtain [20]

$$R = \exp(2i\beta_1 z_0)\left[r_{12} + \frac{t_{12}r_{21}t_{21}\exp(2i\beta_2 d))}{1 - r_{21}^2\exp(2i\beta_2 d)}\right], \quad \text{(A7a)}$$

$$T_s = \exp[i(\beta_1 + \beta_2)z_0]\left[\frac{t_{12}}{1 - r_{21}^2\exp(2i\beta_2 d)}\right], \quad \text{(A7b)}$$

$$R_s = \exp[i(\beta_1 + \beta_2)z_0]\left[\frac{t_{12}r_{21}\exp[2i\beta_2(d - z_0)]}{1 - r_{21}^2\exp(2i\beta_2 d)}\right]. \quad \text{(A7c)}$$

The coefficient of transmission T is given in Eq. (3). Equations (5) and (6) provide the coefficients r_{jk} and t_{jk} for a single interface, respectively.

The analysis given above is fully consistent with Maxwell's equations. Finally, it is straightforward to verify that inserting Eq. (A3) into Eq. (A6) leads to the 2D convolution given in Eq. (1).

This research was funded by the Ministerio de Ciencia e Innovación (MICIIN) under the project TEC2009-11635.

References

1. J. B. Pendry, "Negative refraction makes a perfect lens," Phys. Rev. Lett. **85**, 3966–3969 (2000).
2. V. G. Veselago, "The electrodynamics of substances with simultaneously negative values of ϵ and μ," Phys. Uspekhi **10**, 509–514 (1968).
3. N. Garcia and M. Nieto-Vesperinas, "Left-handed materials do not make a perfect lens," Phys. Rev. Lett. **88**, 207403 (2002).
4. D. R. Smith, D. Schurig, M. Rosenbluth, and S. Schultz, "Limitations on subdiffraction imaging with a negative refractive index slab," Appl. Phys. Lett. **82**, 1506–1508 (2003).

5. S. Cummer, "Simulated causal subwavelength focusing by a negative refractive index slab," Appl. Phys. Lett. **82**, 1503–1505 (2003).
6. A. A. Houck, J. B. Brock, and I. L. Chuang, "Experimental observations of a left-handed material that obeys Snell's law," Phys. Rev. Lett. **90**, 137401 (2003).
7. J. B. Brock, A. A. Houck, and I. L. Chuang, "Focusing inside negative index materials," Appl. Phys. Lett. **85**, 2472–2474 (2004).
8. K. Aydin, I. Bulu, and E. Ozbay, "Focusing of electromagnetic waves by a left-handed metamaterial flat lens," Opt. Express **13**, 8753–8759 (2005).
9. E. Shamonina, V. A. Kalinin, K. H. Ringhofer, and L. Solymar, "Imaging, compression and Poynting vector streamlines with negative permittivity materials," Electron. Lett. **37**, 1243–1244 (2001).
10. M. Nieto-Vesperinas, "Problem of image superresolution with a negative-refractive-index slab," J. Opt. Soc. Am. A **21**, 491–498 (2004).
11. S. A. Ramakrishna, J. B. Pendry, M. C. K. Wiltshire, and W. J. Stewart, "Imaging the near field," J. Mod. Opt. **50**, 1419–1430 (2003).
12. N. Fang, H. S. Lee, C. Sun, and X. Zhang, "Sub-diffraction-limited optical imaging with a silver superlens," Science **308**, 534–537 (2005).
13. R. Kotyński and T. Stefaniuk, "Comparison of imaging with sub-wavelength resolution in the canalization and resonant tunnelling regimes," J. Opt. A: Pure Appl. Opt. **11**, 015001 (2009).
14. M. Born and E. Wolf, *Principles of Optics*, seventh (expanded) ed. (Cambridge, 1999).
15. R. Merlin, "Analytical solution of the almost-perfect-lens problem," Appl. Phys. Lett. **84**, 1290–1293 (2004).
16. M. W. Feise and Y. S. Kivshar, "Sub-wavelength imaging with a left-handed material flat lens," Phys. Lett. A **334**, 326–330 (2005).
17. T. Hakkarainen, T. Setälä, and A. T. Friberg, "Subwavelength electromagnetic near-field imaging of point dipole with metamaterial nanoslab," J. Opt. Soc. Am. A **26**, 2226–2234 (2009).
18. R. Marques, M. J. Freire, and J. D. Baena, "Theory of three-dimensional subdiffraction imaging," Appl. Phys. Lett. **89**, 211113 (2006).
19. M. F. Juette, T. J. Gould, M. D. Lessard, M. J. Mlodzianoski, B. S. Nagpure, B. T. Bennett, S. T. Hess, and J. Bewersdorf, "Three-dimensional sub-100 nm resolution fluorescence microscopy of thick samples," Nature Methods **5**, 527–529 (2008).
20. P. Yeh, *Optical Waves in Layered Media* (Wiley, 1988).
21. K. Miyamoto and E. Wolf, "Generalization of the Maggi–Rubinowicz theory of the boundary diffraction wave—Part I," J. Opt. Soc. Am. **52**, 615–625 (1962).
22. E. Collet and E. Wolf, "Symmetry properties of focused fields," Opt. Lett. **5**, 264–266 (1980).
23. C. W. McCutchen, "Generalized aperture and the three-dimensional diffraction image," J. Opt. Soc. Am. **54**, 240–242 (1964).
24. B. Wood, J. B. Pendry, and D. P. Tsai, "Directed subwavelength imaging using a layered metal-dielectric system," Phys. Rev. B **74**, 115116 (2006).
25. D. de Ceglia, M. A. Vincenti, M. G. Cappeddu, M. Centini, N. Akozbek, A. Dorazio, J. W. Haus, M. J. Bloemer, and M. Scalora, "Tailoring metallodielectric structures for superresolution and superguiding applications in the visible and near-IR ranges," Phys. Rev. A **77**, 033848 (2008).
26. C. Girard and A. Dereux, "Near-field optics theories," Rep. Prog. Phys. **59**, 657–699 (1996).
27. W. T. Welford, "Use of annular apertures to increase focal depth," J. Opt. Soc. Am. **50**, 749–753 (1960).
28. S. Grill and E. H. K. Stelzer, "Method to calculate lateral and axial gain factors of optical setups with a large solid angle," J. Opt. Soc. Am. A **16**, 2658–2665 (1999).